NeuroImage 168 (2018) 321–331

Contents lists available at ScienceDirect

NeuroImage

journal homepage: www.elsevier.com/locate/neuroimage

A method for the dynamic correction of B_0-related distortions in single-echo EPI at 7 T

Barbara Dymerska [a], Benedikt A. Poser [b], Markus Barth [c], Siegfried Trattnig [a], Simon D. Robinson [a,*]

[a] High Field MR Centre, Department of Biomedical Imaging and Image-guided Therapy, Medical University of Vienna, Vienna, Austria
[b] Department of Cognitive Neuroscience, Faculty of Psychology and Neuroscience, Maastricht University, Netherlands
[c] Centre for Advanced Imaging, The University of Queensland, Brisbane, Australia

ARTICLE INFO

Article history:
Received 29 April 2016
Received in revised form
21 June 2016
Accepted 4 July 2016
Available online 7 July 2016

Keywords:
Field mapping
Dynamic distortion correction
Ultra-high field
EPI
fMRI

ABSTRACT

We propose a method to calculate field maps from the phase of each EPI in an fMRI time series. These field maps can be used to correct the corresponding magnitude images for distortion caused by inhomogeneity in the static magnetic field. In contrast to conventional static distortion correction, in which one 'snapshot' field map is applied to all subsequent fMRI time points, our method also captures dynamic changes to B_0 which arise due to motion and respiration. The approach is based on the assumption that the non-B_0-related contribution to the phase measured by each radio-frequency coil, which is dominated by the coil sensitivity, is stable over time and can therefore be removed to yield a field map from EPI.

Our solution addresses imaging with multi-channel coils at ultra-high field (7 T), where phase offsets vary rapidly in space, phase processing is non-trivial and distortions are comparatively large. We propose using dual-echo gradient echo reference scan for the phase offset calculation, which yields estimates with high signal-to-noise ratio. An extrapolation method is proposed which yields reliable estimates for phase offsets even where motion is large and a tailored phase unwrapping procedure for EPI is suggested which gives robust results in regions with disconnected tissue or strong signal decay.

Phase offsets are shown to be stable during long measurements (40 min) and for large head motions. The dynamic distortion correction proposed here is found to work accurately in the presence of large motion (up to 8.1°), whereas a conventional method based on single field map fails to correct or even introduces distortions (up to 11.2 mm). Finally, we show that dynamic unwarping increases the temporal stability of EPI in the presence of motion.

Our approach can be applied to any EPI measurements without the need for sequence modification.

Introduction

fMRI benefits from the use of ultra-high field (UHF) through higher SNR and increased BOLD signal changes (Beisteiner et al., 2011; van der Zwaag et al., 2009). Echo planar imaging (EPI) is, however, sensitive to inhomogeneities in the static magnetic field, B_0, that arise from the interfaces between tissues with differing magnetic susceptibilities and which increase linearly with B_0. Inhomogeneities in B_0 cause geometric distortions in EPI in the phase-encoding direction (Jezzard and Balaban, 1995) which lead to mislocalization of activation and difficulty coregistering functional results to anatomical scans (Cusack et al., 2003; Gartus et al., 2006). Distortions can be corrected using a B_0 field map calculated from the phase change between images acquired at different echo times (TEs) (Jezzard and Balaban, 1995). A single field map does not, however, capture dynamic changes in B_0 that occur during the fMRI acquisition due to motion (Jezzard and Clare, 1999), respiration (Zahneisen et al., 2014; Zeller et al., 2013) and heating of the gradient system (Foerster et al., 2005).

A number of dynamic distortion correction (DDC) methods have been presented. Hutton et al. proposed modelling the phase changes due to motion and gradient heating (Hutton et al., 2013), assuming that phase changes are linear with head motion and relatively small. This is not necessarily the case at UHF, especially during long measurements and paradigms with task-related motion. Andersson et al. (2001) modeled relative geometric deformations from EPI magnitude image intensities and motion parameters taking into account movement-by-susceptibility interactions, but neglecting other sources of geometric distortions such as respiration.

A field map can be generated for each time point if multi-echo EPI is used (Hutton et al., 2002; Visser et al., 2012; Weiskopf et al.,

* Corresponding author at: High Field MR Centre, Medical University of Vienna, Lazarettgasse 14, A-1090 Vienna, Austria.
E-mail address: simon.robinson@meduniwien.ac.at (S.D. Robinson).

https://doi.org/10.1016/j.neuroimage.2016.07.009

2005), but this limits the achievable spatial resolution (Poser and Norris, 2009). Dynamic field maps can also be calculated between adjacent time points if the TE is alternated between different values for odd and even time points (Dymerska et al., 2015). This is reliable if the echo times are well chosen, but a DDC solution which did not require changes to the EPI sequence would present a clear advantage.

The phase measured with a radiofrequency (RF) coil comprises an offset, which is dominated by the coil sensitivity, and a component which is proportional to B_0 and TE (Robinson et al., 2011). A time series of 'dynamic' field maps can therefore be generated by subtracting the phase offset from the total phase measured at each EPI time point. This approach, which requires no change to the conventional, single-echo EPI sequence, was proposed by Marques and Bowtell (2005) and Lamberton et al. (2007). These papers do not address how to combine phase data from the multiplicity of coils used in a modern phased array, however. Each coil element is subject to a different offset, $\varphi_{0,ch}$, which is spatially heterogeneous at UHF (Collins, 2006) and needs to be reliably determined from inhomogeneous single-channel data. Prior work also has not considered errors in the estimates of φ_0 that occur when the field changes during the reference measurement (Dymerska et al., 2015; Zahneisen et al., 2014; Zeller et al., 2013) or when there is substantial movement during the fMRI time series. The most challenging step in single-echo DDC, however, is the reliable unwrapping of each EPI phase image. Hahn et al. and Ooi et al. showed that at low and intermediate field (up to 3 T), the unwrapping problem can be circumvented by considering only the differences between each EPI and a reference image (Hahn et al., 2009; Ooi et al., 2012). Dynamic deformations are corrected with respect to the reference image, but a second unwarping, using a reference field map, is needed in order to remove all distortions.

The aim of this study was to develop a single-echo DDC approach that works with multi-channel coils at 7 T and is robust to head rotations of several degrees. Our solution is based on a dual-echo Gradient Echo (GE) reference acquisition which yields more reliable estimates of $\varphi_{0,ch}$ than the EPI-based measurements used in previous work (Lamberton et al., 2007; Marques and Bowtell, 2005). GE-based phase offsets also minimize respiration-related field errors which arise when EPI with different echoes are acquired at different time points (Dymerska et al., 2015; Zahneisen et al., 2014; Zeller et al., 2013). The extrapolation method we propose is suitable for spatially heterogeneous phase offsets, which allows optimal combination of separate-channel phase information in the presence of motion. An unwrapping procedure for EPI phase data is described which substantially reduces errors in disconnected tissue areas and regions with a strong signal decay. The temporal stability of φ_0 at 7 T during long measurements and in the presence of large motion is investigated for the first time. This DDC approach is compared with a static distortion correction (SDC) approach in the presence of head rotations up to circa 8°.

Theory

The errors encountered with different field mapping approaches are considered here, for a single RF coil, before proposing a solution for multi-channel data using separate-channel phase offsets.

Error estimation in three different field mapping approaches

The phase φ at a given time t and echo time TE comprises a TE-independent phase offset, φ_0 and a term describing local deviations from the static magnetic field, ΔB_0 (here in Hz):

$$\varphi(x,y,z,t) = \varphi_0(x,y,z,t) + 2\pi TE\cdot\Delta B_0(x,y,z,t), \quad (1)$$

where x,y,z are the spatial coordinates (Robinson et al., 2011). Noise and wraps are neglected, as are comparatively small, non-linear contributions to the phase (Wharton and Bowtell, 2012).

Consider two scans: a dual-echo 'reference' scan with TE_1 and TE_2 that will provide information for field map generation and a single-echo scan with TE_3, the target to be distortion corrected with the field map. Optimally, we would like to obtain the field map (ΔB_0^{target}) exclusively from the second scan. This is not possible, however, since it is a single-echo acquisition. We therefore consider three ways in which ΔB_0^{target} can be approximated (case I, II and III): I) from the phase difference between the two echoes of the reference scan, II) from the phase difference between the target scan and one echo from the reference scan and III) by taking the target image at TE_3 and subtracting a phase offset estimated from the reference scan. In general there may be a change in the field between the reference scan and the target scan; $\Delta B_0^{target}=\Delta B_0^{ref}+\delta B_0$, and a change in phase offset; $\varphi_0^{target}=\varphi_0^{ref}+\delta\varphi_0$, due to motion, gradient heating, etc. In case I a field map estimated exclusively from the reference scan, thus reads:

$$\Delta B_0^{I} = \Delta B_0^{ref} = \Delta B_0^{target} - \delta B_0 \quad (2)$$

The field map in case II is:

$$\begin{aligned}\Delta B_0^{II} &= \frac{\varphi^{target}-\varphi^{ref}}{2\pi(TE_3-TE_1)} = \\ &= \frac{\varphi_0^{target}+2\pi TE_3\cdot\Delta B_0^{target}-\left(\varphi_0^{target}-\delta\varphi_0\right)-2\pi TE_1\cdot\left(\Delta B_0^{target}-\delta B_0\right)}{2\pi(TE_3-TE_1)} = \\ &= \Delta B_0^{target}+\frac{TE_1}{(TE_3-TE_1)}\delta B_0+\frac{\delta\varphi_0}{2\pi(TE_3-TE_1)}\end{aligned} \quad (3)$$

and in case III:

$$\begin{aligned}\Delta B_0^{III} &= \frac{\varphi^{target}-\varphi_0^{ref}}{2\pi TE_3} = \frac{\varphi_0^{target}+2\pi TE_3\cdot\Delta B_0^{target}-\left(\varphi_0^{target}-\delta\varphi_0\right)}{2\pi TE_3} \\ &= \Delta B_0^{target}+\frac{\delta\varphi_0}{2\pi TE_3}\end{aligned} \quad (4)$$

The errors in the field map for the three cases are: I) $-\delta B_0$, II) $\frac{TE_1}{(TE_3-TE_1)}\delta B_0+\frac{\delta\varphi_0}{2\pi(TE_3-TE_1)}$ and III) $\frac{\delta\varphi_0}{2\pi TE_3}$. It is worth noting that $\frac{\delta\varphi_0}{2\pi TE_3}$ is usually much smaller than δB_0 because the phase offset does not depend on local (e.g. blood oxygenation) or external (e.g. lung volume) susceptibility changes or head orientation with respect to B_0. The head position with respect to the coils affects $\delta\varphi_0$, but this leads to changes in $\frac{\delta\varphi_0}{2\pi TE_3}$ which are typically around 100 times smaller than those in δB_0, as will be shown in the Results (Exp. 2). The field mapping errors are hence the smallest in case III, the approach we adopted here. This scenario is extended to the corresponding field map equation for multi-channel data.

Derivation of a field map equation for a dynamic distortion correction from multi-channel data

The phase measured with each RF coil in a phased array, φ_{ch}, consists of a channel-dependent phase offset, $\varphi_{0,ch}$, and a field-dependent term, ΔB_0, that is common to all channels:

$$\varphi_{ch}(x,y,z,t) = \varphi_{0,ch}(x,y,z,t) + 2\pi TE\cdot\Delta B_0(x,y,z,t) \quad (5)$$

Phase offsets need to be estimated from the dual-echo reference scan in order to calculate a field map at each time point t in a target measurement, i.e. an EPI time series. The first step in this is to calculate a field map from the separate-channel reference data:

$$\Delta B_0^{ref}(x,y,z) = \frac{\angle\left[\sum_{ch} M^{ref}_{ch,TE_2}(x,y,z)\cdot M^{ref}_{ch,TE_1}(x,y,z)\cdot e^{i\left(\varphi^{ref}_{ch,TE_2}(x,y,z)-\varphi^{ref}_{ch,TE_1}(x,y,z)\right)}\right]}{2\pi\cdot(TE_2-TE_1)} \quad (6)$$

where the numerator is the Hermitian inner product (Bernstein et al., 1994) with separate channel magnitude M^{ref}_{ch} and phase φ^{ref}_{ch} images at two echo times TE_1 and TE_2, and $\angle$ symbolizes the four-quadrant tangent inverse (here of the complex sum). The phase offsets can then be calculated by the channel-wise subtraction of the scaled ΔB_0^{ref} from the separate channel phase images, φ^{ref}_{ch}, at TE_1 (since it has higher SNR than that at TE_2):

$$\varphi^{ref}_{o,ch}(x,y,z) = \angle e^{i\left(\varphi^{ref}_{ch,TE_1}(x,y,z)-2\pi TE_1\cdot\Delta B_0^{ref}(x,y,z)\right)} \quad (7)$$

The phase offsets are subsequently subtracted channel-by-channel from the phase of the target scan at each time point t, resulting in the final expression for dynamic field maps using magnitude (M^{target}_{ch}) and phase (φ^{target}_{ch}) information and echo time (TE) from a target single-echo EPI:

$$\Delta B_0^{target}(x,y,z,t) = \frac{\angle\left[\sum_{ch} M^{target}_{ch}(x,y,z,t)\cdot e^{i\left(\varphi^{target}_{ch}(x,y,z,t)-\varphi^{ref}_{o,ch}(x,y,z)\right)}\right]}{2\pi\cdot TE}, \quad (8)$$

where $\varphi^{ref}_{o,ch}(x,y,z)$ are estimated from the reference scan. In order to avoid unnecessary noise enhancement in ΔB_0^{target} and problems at the brain boundaries, the phase offsets are additionally smoothed and extrapolated outside the brain before use in Eq. (8). This process is described in the methods section.

A field map can be converted to a voxel shift map (VSM), which describes by how many voxels each voxel should be shifted to regain its true location:

$$VSM(x,y,z,t) = \frac{\Delta B_0^{target}(x,y,z,t)}{RBW_{PE}\cdot R}, \quad (9)$$

where RBW_{PE} is the receiver bandwidth in the phase-encode direction and R is the in-plane parallel imaging acceleration factor.

Methods

Image acquisition

Measurements were performed with a 7 T whole body Siemens Magnetom scanner (Siemens Healthcare, Erlangen, Germany) and a 32-channel head coil (Nova Medical, Wilmington, Massachusetts, USA).

Two experiments were designed to test the temporal stability of phase offsets with respect to gradient heating and volunteer head motion. A third experiment was conducted to test the single-echo DDC method proposed here, assessing the accuracy of the correction and the effect on temporal SNR (tSNR). Volunteers participated with written informed consent to the studies, which were approved by the Ethics Committee of the Medical University of Vienna.

Experiment 1: evaluation of phase offset temporal stability with respect to gradient heating using EPI

A spherical oil phantom was imaged with four consecutive dual-echo EPI time series, each of 10 min duration (total of 40 min), with TR = 2500 ms (240 volumes/run), TE = [11, 30] ms, RBW = 1502 Hz/pixel (in read-out direction), matrix size = 64 × 64, 3 slices, 10% gap, voxel dimensions = 3.3 × 3.3 × 3.5 mm^3, FA = 75°, GRAPPA 2 and 6/8 partial Fourier.

Experiment 2: evaluation of phase offset temporal stability in the presence of large head motion using GE

One volunteer (30 year-old male, denoted V1) was asked to perform a head rotation (of up to 12°) around a left-right axis in 8 steps. The motion was performed in between the measurements but not during them. Dual-echo gradient echo images were acquired for the estimation of $\varphi_{0,ch}$ at each head position (8 poses). The following parameters were used: TR = 398 ms, TE = [2.5, 5.0] ms, RBW = 540 Hz/pixel, matrix size = 138 × 138, 33 slices, 50% gap, voxel dimensions = 1.6 × 1.6 × 2 mm^3, FA = 36°, GRAPPA 4, 6/8 partial Fourier.

Experiment 3: analysis of the quality of the dynamic distortion correction and the effect of the correction on tSNR

Five scans were acquired for each of three volunteers (V1: 30 year-old male, V2: 31 year-old female, V3: 25 year-old male): i) two dual-echo GE acquisitions for static field map calculation and phase offset estimation, ii) one single-echo GE scan, to serve as a nearly distortion-free reference and iii) two single-echo EPI time-series of 24 time points; the target scans to be distortion corrected. Volunteers were asked to lie still during the first EPI run and to perform a head rotation about the left-right axis during the second. The dual-echo GE scans were acquired twice, once with anterior-posterior phase-encode direction and once with posterior-anterior phase-encoding direction to allow elimination of gradient delay effects (Reeder et al., 1999). All measurements were performed with matrix size = 138 × 138, 33 slices, 25% gap, voxel dimensions = 1.6 × 1.6 × 2 mm^3, GRAPPA 2, 6/8 partial Fourier. The remaining sequence parameters were: i) TR = 600 ms, TE = [2.5, 5.0] ms, RBW = 510 Hz/pixel, FA = 43° ii) TR = 1000 ms, TE = 22 ms, RBW = 557 Hz/pixel, FA = 54° iii) TR = 2000 ms, TE = 22 ms, RBW = 1510 Hz/pixel, FA = 70° with ascending slice acquisition. The posterior-anterior phase encoding direction was chosen for EPI (i.e. the phase encoding pre-winder is negative), to have signal stretch rather than pile-up in the orbitofrontal cortex (De Panfilis and Schwarzbauer, 2005).

Data analysis

Data processing was performed with MATLAB (MathWorks, Natick, Massachusetts, USA) unless otherwise specified. Phase unwrapping was carried out in 2D with PRELUDE v2.0 from the FSL library (Jenkinson, 2003). In the case of EPI, additional unwrapping steps were implemented in MATLAB, as described in the subsection of Exp. 3. GE data were masked with FSL's BET (Smith, 2002) and EPI data using the SPM 8 New Segment tool (www.fil.ion.ucl.ac.uk/spm/software/spm8/), which creates probability maps for cerebrospinal fluid, white and gray matter. Summing these three maps together and setting values ≥ 0.5 to 1 and < 0.5 to 0 yielded a binary mask. This was found to be more reliable than FSL BET in this application. Phase offsets and field maps were smoothed using a discretized spline smoother (MATLAB function smoothn.m (Garcia, 2010)). When extrapolation of the values outside the brain was required, background values were padded with NaNs to cause smoothn.m to treat these as missing values and iteratively extrapolate values for these voxels based on a discrete cosine transform (for more information see "Dealing with weighted data and occurrence of missing values" in (Garcia, 2010)). Processing steps which were specific to the experiment are described in the following three subsections.

Experiment 1: evaluation of phase offset temporal stability with respect to gradient heating using EPI

For each dual-echo EPI frame the Hermitian inner product (the

numerator in Eq. (6)) was calculated and unwrapped. Residual phase jumps of integer multiples of 2π were removed between consecutive slices and time points (Robinson and Jovicich, 2011). Resulting phase images were divided by $2\pi\Delta TE$ to yield a field map in Hz for each frame. The $\varphi_{0,ch}$ were obtained by the subtraction of the scaled field map (ΔB_0) for that time point from the first echo (at 11.0 ms) of the separate channel phase, as in Eq. (7). A relative change in $\varphi_{0,ch}$ was calculated with respect to the first volume. The mean change of $\varphi_{0,ch}$ was computed channel-wise within the phantom (using a mask) with additional exclusion of the voxels with the maximum intensity $< 10\%$ in the separate channel magnitude image: low signal regions in separate channel data contribute negligibly to the combined image, but tend to have a large temporal standard deviation, since the noise voxels in phase have the same range of values as the signal voxels (Vegh et al., 2015).

Experiment 2: evaluation of phase offset temporal stability in the presence of large head motion using GE

Field maps and phase offsets were calculated for each head Pose (1 to 8) following the same steps as in Exp.1 (here using dual-echo GE instead of EPI). Each $\varphi^{ref}_{o,ch}$ was split into a weighted real ($M^{ref}_{ch}\cdot\cos(\varphi^{ref}_{o,ch})$) and imaginary part ($M^{ref}_{ch}\cdot\sin(\varphi^{ref}_{o,ch})$). Both parts were smoothed and extrapolated outside the brain with smoothing parameter equal to 2 (in the MATLAB function smoothn.m) before converting back to phase to generate the final version of the phase offsets. The above process of splitting, smoothing, and combining back allows interpolation artifacts close to wraps in the $\varphi^{ref}_{o,ch}$ to be avoided (Robinson et al., 2015).

Combined phase images were reconstructed as described in the numerator of Eq. (8), where phase offsets originated from the target scan ($ref = target$) or from the first scan ($ref = Pose\ 1$). The first case ($ref = target$) reflects the 'optimal solution'. The second case ($ref = Pose\ 1$) is the 'approximate solution' used in the method proposed here, which assumes that changes in phase offsets between the reference and the target have a small effect on field maps. Motion was estimated, but not corrected, using the SPM 8 motion estimation tool.

Experiment 3: analysis of the quality of the dynamic distortion correction and the effect of the correction on tSNR

The analysis performed in Exp. 3 is schematically shown in Fig. 1, which shows 4 of the 32 coil elements for illustration. As in Exp. 2, a GE field map (Fig.1, 'A') and extrapolated phase offsets (Fig.1, 'D') were calculated.

In order to perform the SDC, the GE field map was masked, smoothed with a smoothing parameter value of 0.5 and converted to a VSM (see Eq. (9)). This VSM was applied to the GE field map to bring the GE spatial coordinates to the distorted EPI space. This process we denote as forward warping (Fig. 1, 'B'). The smoothing and the conversion to VSM were repeated on the forward-warped GE field map to yield the final VSM used for SDC (see Eq. (9) and Fig. 1, 'C').

In the pipeline for the DDC, extrapolated phase offsets derived from the GE data were subtracted from the separate channel EPI phase (Fig. 1, 'E') to yield matched phases (Fig. 1, 'F'), which were combined using the complex sum (see the numerator of Eq. (8)) and unwrapped in a number of steps which are illustrated in the bottom right of Fig. 1: unwrapping within a brain mask using 2D PRELUDE and a triplanar approach (Robinson et al., 2014) in the regions with disconnected tissue, for instance in last few dorsal slices. These results were then smoothed and extrapolated outside the brain (smoothing parameter = 2) and made congruent to the unmasked wrapped phase. In the congruence operation the difference between the unwrapped and wrapped phase was rounded to integer multiplies of 2π and added to the wrapped phase to yield the final unwrapped image. This multi-step unwrapping procedure was used to remove unwrapping errors at the brain boundaries and in the regions with low signal (e.g. close to sinuses) and to create a smooth image background. Unwrapped combined phase images were divided by $2\pi TE$ to yield a time series of field maps, which were smoothed (smoothing parameter = 0.5) and converted into VSMs (see Eq. (9) and Fig. 1, 'G').

SDC and DDC were performed on magnitude EPI data using the corresponding static and dynamic VSMs. Since voxel shifts are often non-integer, linear interpolation in the phase-encode direction (MATLAB function interp1.m) was used to bring the unwarped data to the original 138×138 grid. To allow the final distortion correction results to be assessed, the original combined magnitude EPI data and the same data which had been unwarped with SDC and DDC and were motion-corrected to the distortion-free GE reference (with TE = 22 ms) using the rigid body realignment tool in SPM 8. Visual comparison of EPI and GE data allowed residual distortions to be regionally assessed with the MRIcro software (http://people.cas.sc.edu/rorden/mricro/index.html). Additionally, temporal standard deviation (tSD) and tSNR maps were calculated from the original (noDC), SDC and DDC data. Chi-squared two sample tests were performed for each subject for tSD and tSNR for both the motion and no motion conditions: the null hypothesis was that tSD and tSNR results from i) noDC and SDC datasets or ii) noDC and SDC datasets come from the same distribution.

Results

Experiment 1: evaluation of phase offset temporal stability with respect to gradient heating using EPI

There was no substantial drift in phase offsets during 40 min of dual-echo EPI: the mean change in $\varphi_{0,ch}$ with respect to the first volume did not exceeded 0.1 ± 0.2 rad. If $\varphi_{0,ch}$ from the first time point were to be used to calculate field maps for the DDC of a single-echo time series, the variation observed in $\varphi_{0,ch}$ would lead to a voxel shift error not larger than 0.1 voxel with the EPI parameters used in Exp.3.

Experiment 2: evaluation of phase offset temporal stability in the presence of large head motion using GE

The subject rotated their head by a total of 12.0° between Pose 1 and Pose 8. A large number of voxels were in noise (background) in Pose 1 but in signal (tissue) in later poses, or vice versa, particularly in the most ventral and dorsal slices. For slices from 1 to 6 this value change (of noise to tissue) affected about 14% of the tissue voxels. For slices from 25 to 28 (one of the last dorsal slices) the corresponding value was around 29%. As a result, effective extrapolation of $\varphi_{0,ch}$ values was required for those voxels.

Column 2 in Fig. 2 illustrates phase combination results for Pose 6 and 8 in one ventral slice (Slice 6, top half of figure) and one dorsal slice (Slice 26, bottom half of figure) using the optimal solution, where the phase offsets were derived from the target Pose (6 or 8) and brain boundaries in the $\varphi_{0,ch}$ perfectly match those in separate channel phase images (φ_{ch}). Column 3 in Fig. 2 shows the approximate solution (i.e. the proposed method), where $\varphi_{0,ch}$ from Pose 1 were used to reconstruct the phase of Pose 6 or 8 and missing values in $\varphi_{0,ch}$ were estimated using extrapolation (see the Data analysis section). Differences between the approximate and the optimal solution have been converted into voxel shift errors

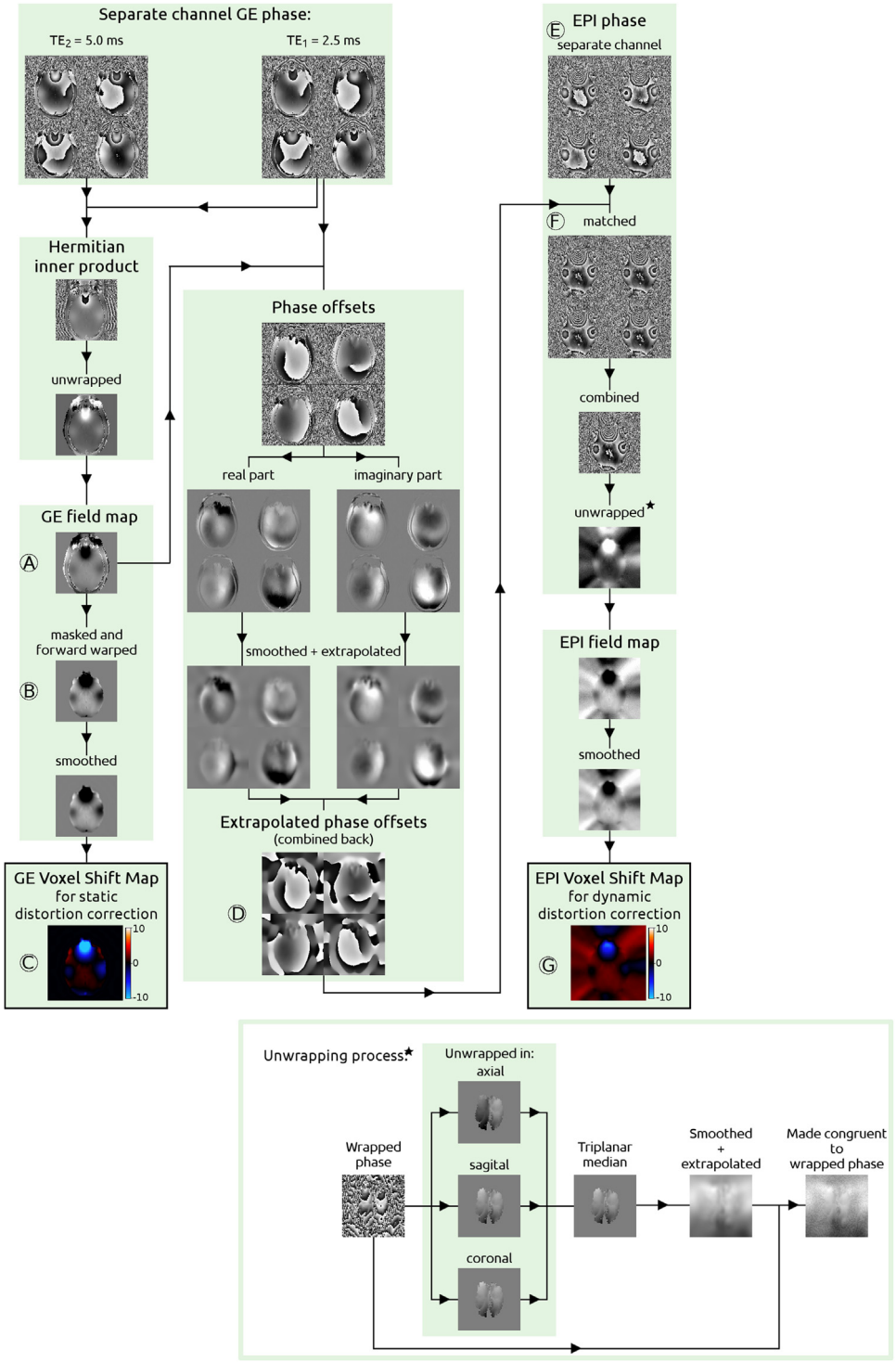

Fig. 1. Processing steps used in Exp. 3 to obtain voxel shift maps used for the SDC and DDC of EPI proposed here. For simplification, 4 out of 32 channels are shown. At the bottom right of the image unwrapping steps applied to the EPI phase (but not to GE phase) are presented. Capital letters (A–G) mark the steps described in the text.

based on sequence parameters in Exp. 3 and are presented in the 4th column of Fig. 2. These errors reached a maximum of 0.1 voxels in slice 6 and −0.2 voxels in slice 26 for head rotation of 12° (indicated in Fig. 2 by arrows 3 and 5 respectively). In contrast, using a field map from Pose 1 to correct distortions in Pose 8 (as in SDC) would cause errors of up to 11.4 voxels in slice 6 and 6.9 voxels in slice 26 (see arrows 4 and 6 respectively). The above was estimated from a difference between field maps from Pose 8 and 1. The errors for Pose 6, with head rotation of 6.3°, were slightly smaller; the approximate DDC solution led to errors of up to 0.1 voxel (at arrow 1) and ΔB_0 difference between Pose 6 and 1 reached up to 9.1 voxels (at arrow 2). For head rotation of 2.0° (Pose 2) the approximate solution was characterized by errors below 0.1 voxels, while ΔB_0 differences between Pose 2 and 1 reached up to 3.2 voxels (results not shown).

Experiment 3: analysis of the quality of the dynamic distortion correction and the effect of the correction on tSNR

Fig. 3 shows a comparison of the SDC and DDC with respect to

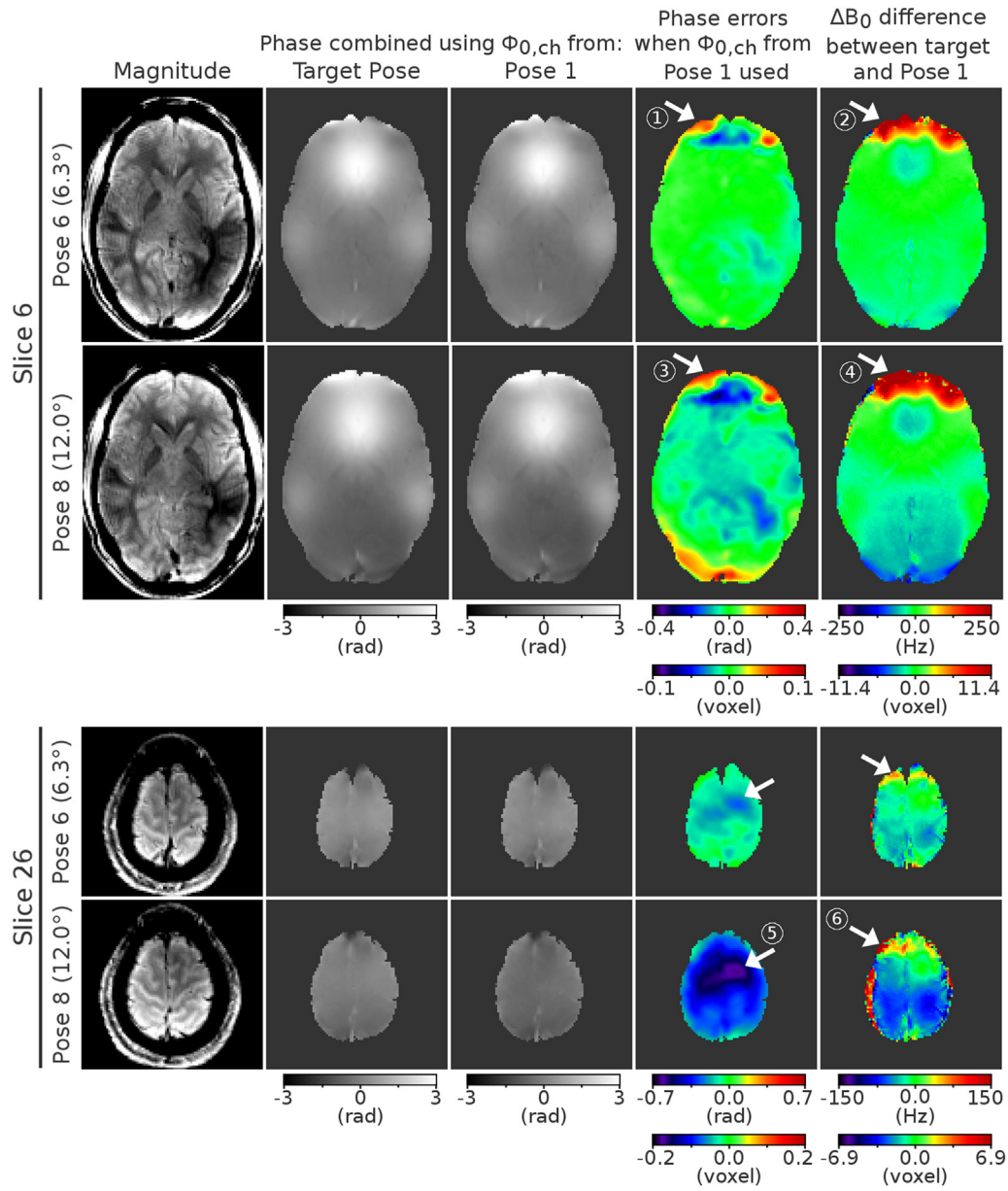

Fig. 2. Estimation of the voxel shift errors introduced by changes to the phase offset and B_0 field in the presence of large motion. Ventral and dorsal slices for Pose 8 with 12.0° and Pose 6 with 6.3° head rotation are shown. Phase images from Pose 6 and 8 combined using the optimal solution (where $\varphi_{0,ch}$ from the target pose are used) and the approximate solution (where the $\varphi_{0,ch}$ from Pose 1 are used) are presented in columns 2 and 3 respectively. Phase errors in the approximate DDC solution are depicted in the 4th column. The difference between the field map at target Pose (6 or 8) and Pose 1 is shown in the 5th column, for comparison. The last represents the errors that would be encountered in SDC. White arrows mark regions where the largest errors would occur in a distortion correction if the approximate DDC solution or SDC (form Pose 1) were used. Note the large difference in scales between columns 4 and 5.

the original distorted EPI (noDC) and GE reference, which is distortion-free in the phase encoding direction. One dorsal and one ventral slice are shown for volunteer V2 at three time points, characterized by three different head rotations (0.8°, 4.1° and 7.0° with respect to the GE reference). Results for the other two volunteers are presented in Supplementary materials (V1: Fig. S1 and V3: Fig. S2).

Residual distortions are apparent in SDC even when only 0.8° rotation occurred between the reference field map and EPI. These were up to 1.6 mm (or 1 voxel) in the central sulcus and in the occipital lobe (Fig. 3, arrows 5 and 6 respectively), 3.2 mm (2 voxels) in the frontal lobe dorsally (Fig. 3, arrow 4), and 6.4 mm (4 voxels) in the frontal lobe ventrally (Fig. 3, arrow 1). Distortions increased up to 8.0 mm (5 voxels) for 4.1° head rotation (Fig. 3, arrow 2) and up to 9.6 mm (6 voxels) for 7.0° head rotation (Fig. 3, arrow 3). For the largest motion, the area close to the central sulcus affected by SDC error of about 1.6 mm extended to large parts of the hand knob region (Fig. 3, arrow 7). Additionally, in some regions, SDC led to blurring (as in Fig. S2 in the circle).

No blurring or residual distortions were apparent in dynamically corrected data (see Fig. 3, S1 and S2; 4th column) with the exception of a small region in volunteer V1 where, for 7.9° head rotation, there was an unwrapping error in the combined phase (see Fig. S1, arrow 1) which led to residual distortion of up to 3.4 mm (2 voxels). In comparison, SDC led to errors up to 11.2 mm in the same area (see Fig. S1, arrow 2).

The temporal stability of static and dynamic unwarping is visualized for V1 in a movie available in Supplementary materials. It shows a single GE reference image, original EPI time series (with no motion correction and noDC) and motion-corrected time series

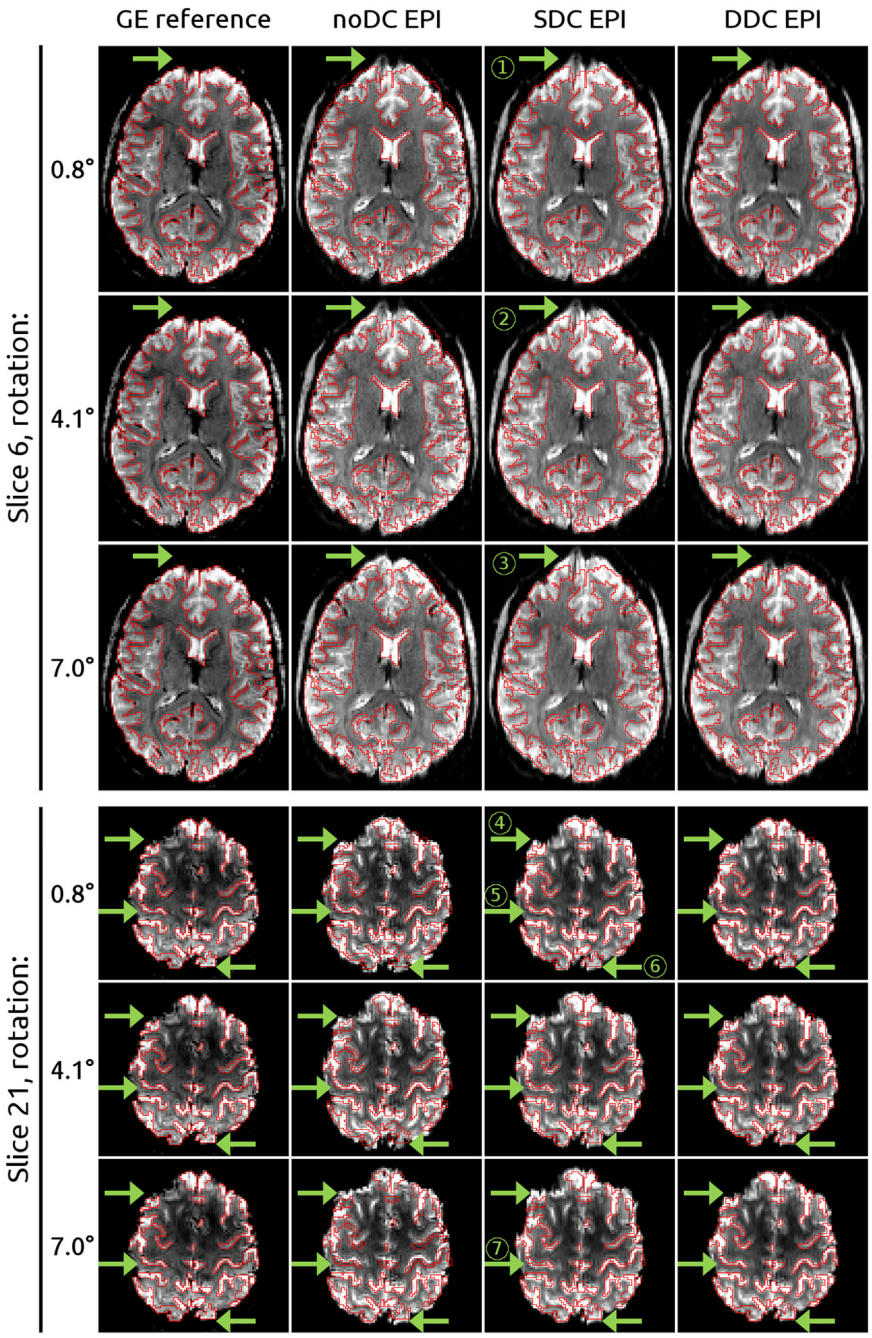

Fig. 3. The accuracy of static (SDC) and dynamic (DDC) distortion correction for volunteer V2 in comparison with original distorted (noDC) EPI and distortion-free reference GE. Two slices (6 and 21) are presented for 3 motion-corrected volumes with estimated rotations of 0.8°, 4.1° and 7.0°. Red outlines were drawn based on the GE reference. Green arrows point to regions where SDC was erroneous and DDC was accurate. (For interpretation of the references to colour in this figure legend, the reader is referred to the web version of this article.)

with noDC, SDC and DDC. The estimated head rotation in each frame is marked in the bottom right corner. Progressive stretching of the noDC EPI in the phase encoding direction with increasing head motion was removed by the DDC but not by SDC. Subtle image intensity fluctuations in noDC, SDC and DDC EPI remain due to imperfect motion correction (which is not optimized for such a large and relatively rapid motion).

Temporal standard deviation and temporal signal-to-noise ratio were quantified for all volunteers for noDC, SDC and DDC EPI with no intentional motion or head rotation. There was no large difference in tSD or tSNR between the datasets with no intentional motion (see Fig. S3 and S4 in Supplementary material). The differences were, however, statistically significant for all volunteers and all conditions ($p < 0.00001$). For V2 there was a small reduction in tSD (median 19, 17, 16 for noDC, SDC and DDC respectively) and an increase in tSNR (median 52, 60, 61) over the whole brain volume (Fig. S4, middle column). In EPI with motion, the tSD was reduced by DDC, particularly in the prefrontal cortex close to the sinuses, marked by arrows in Fig. 4. A general reduction in tSD and increase in tSNR with DDC was observed in the whole brain for all three volunteers, as shown in histograms in Fig. 5. The largest reductions in tSD occurred for volunteer V2, where median tSD was reduced from 82 to 48 by SDC and to 40 by DDC, which lead to a corresponding tSNR increase from 13 to 22 by SDC and to 26 by DDC. In V1 and V3 SDC caused a regional increase in tSD, as marked by circles in dorsal slices in Fig. 4. For V1 median tSD in

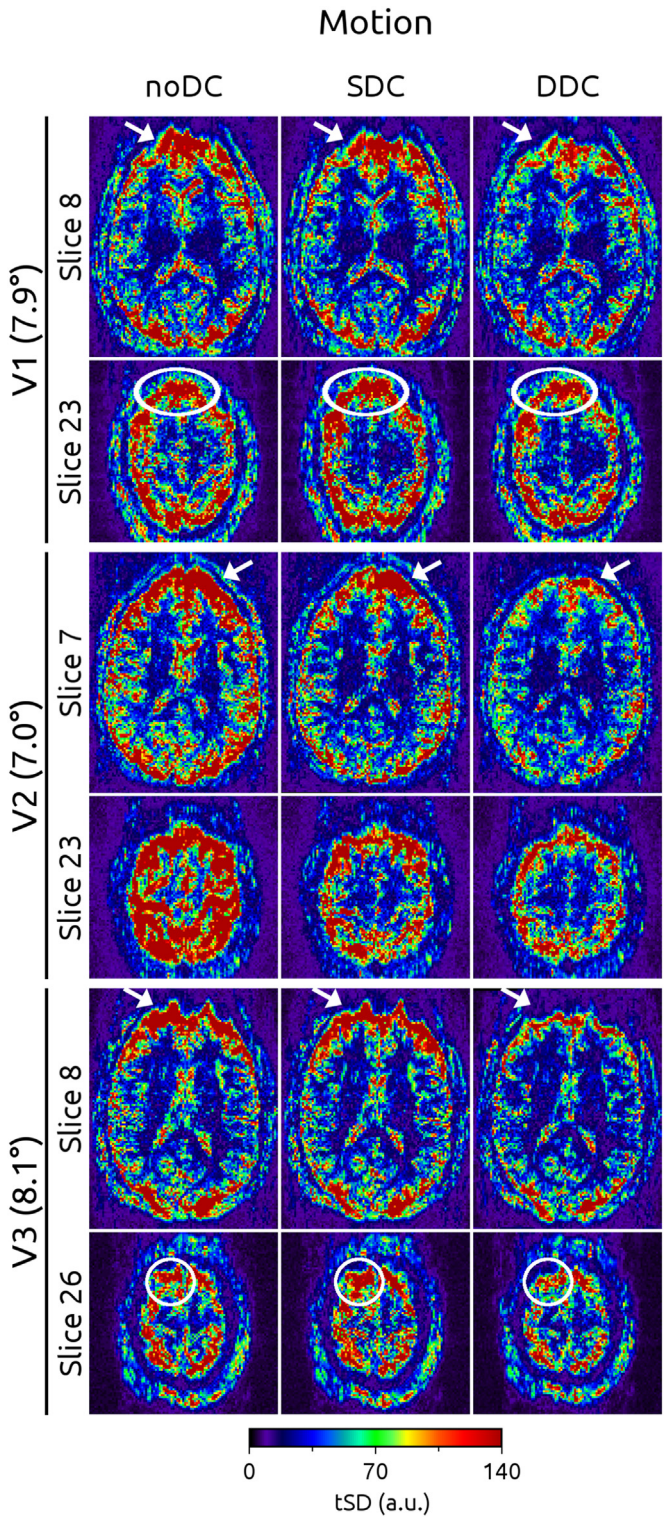

Fig. 4. Comparison of a tSD for all three volunteers between EPI with noDC, SDC and DDC in the presence of intentional motion (maximum rotation written in the brackets). Substantial reduction in tSD is visible after DDC, especially close to brain boundaries. Arrows mark regions with largest tSD reduction by DDC. Circles show regions where SDC increased tSD.

the whole brain volume was 55, 50, 47 and median tSNR was 19, 21, 22 after noDC, SDC and DDC respectively. For V3 median tSD was 43, 44, 33 and median tSNR 21, 21, 26 after noDC, SDC and DDC respectively. As in no motion case, the differences in tSD and tSNR distributions between noDC and SDC or noDC and DDC were statistically significant ($p < 0.00001$).

Discussion

We have proposed a dynamic distortion correction method for conventional, single-echo EPI that is compatible with multi-channel coils at UHF. This approach is based on the approximation that the 'offsets' to the phase measured with each RF coil are stable over long measurements and in the presence of motion. Subtraction of these contributions from the total phase in each EPI volume leaves scaled field maps for each time point which can be used to perform a dynamic distortion correction of the corresponding magnitude images.

Our approach extends prior single-echo EPI-based DDC methods (Lamberton et al. (2007); Marques and Bowtell (2005); Hahn et al. (2009) and Ooi et al. (2012)) by presenting a solution for multi-channel coils at UHF. This is not trivial, as phase offsets - which are both spatially heterogeneous and different for each coil - need to be measured reliably, despite lower SNR in each image, and interpolated to provide robust estimates at the brain boundary. We also present an unwrapping procedure which substantially reduces errors in disconnected tissue areas and regions with a strong signal decay. These elements allow accurate field inhomogeneity estimates from each EPI volume.

In contrast to prior methods we propose measuring phase offsets with a dual-echo Gradient Echo (GE) acquisition. Estimates of phase offsets based on EPI, rather than GE images, are more prone to unwrapping errors due to low SNR. Additionally, if phase offsets are estimated from separate measurements at two time points, as suggested by Lamberton et al. (2007) and Marques and Bowtell (2005), substantial errors occur if the field changes between those two measurements (due to respiration, for instance). This has been demonstrated by Zeller et al. (2013) and Dymerska et al. (2015) and is elucidated in the Theory section here.

The large motion examined in this work made extrapolation of phase offsets necessary and challenging due to extended mismatch between the brain boundaries in the reference $\varphi_{0,ch}$ and target phase. As an alternative to the discretized spline smoother we have used (Garcia, 2010) we have also tested polynomial fitting in Exp. 2, as suggested by Marques and Bowtell (2005) and Lamberton et al. (2007). Phase matching with $\varphi_{0,ch}$ values obtained with different extrapolation procedures was quantified via the Q factor (Robinson et al., 2015); perfect phase matching (Q = 100%) is reflected in accurate field maps. Extrapolation with a third order polynomial gave Q values as low as 50% in ventral slices, where there was strong mismatch in brain boundaries between the reference $\varphi_{0,ch}$ and the target phase. Increasing the polynomial order improved the phase matching but some regions with Q = 75% remained, even if 8th order terms were used. Q values were above 97% throughout the brain with the discretized spline smoother suggested here, even for head rotations as large as 12°. Another possibility is to perform a rigid-body realignment of the $\varphi_{0,ch}$ to each volume of the EPI, which could partially remove the mismatch between the brain boundaries. To fully remove the mismatch a forward warping of the $\varphi_{0,ch}$ to the EPI space would be necessary, which cannot be performed without prior knowledge of ΔB_0 at each time point. A process with the initial estimation of ΔB_0, as here proposed, and iterative forward warping of $\varphi_{0,ch}$ with subsequent re-estimation of ΔB_0 could further improve the matching between the $\varphi_{0,ch}$ and EPI data brain boundaries. Such a solution, however, would substantially increase the computation time and could be more vulnerable to unwrapping errors (since the unwrapping would have to be performed at each iterative step). Our simple solution with no rigid-body realignment and no forward-warping, but with the extrapolation of the $\varphi_{0,ch}$ gave satisfactory results with good phase matching (Q > 97%) and small unwarping errors (below 0.2 voxels for rotations of 12°, see Exp.2).

Unwrapping combined EPI phase is challenging in regions with

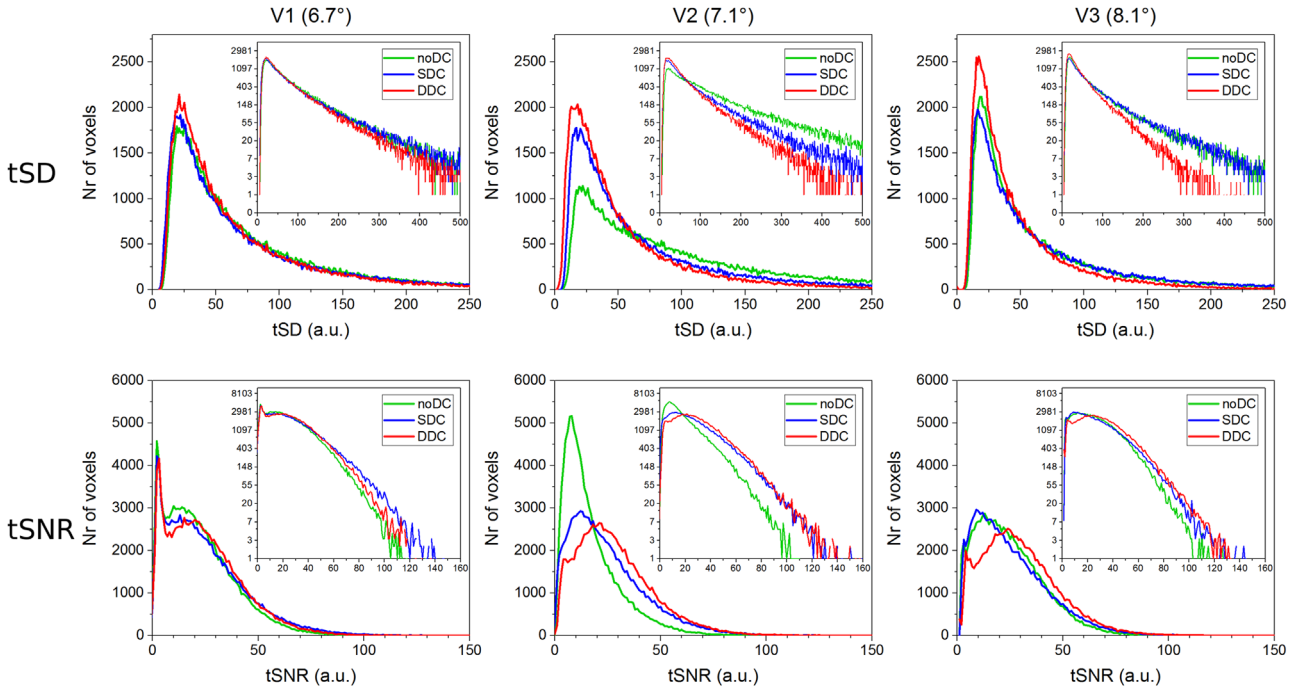

Fig. 5. Histograms comparing tSD (top row) and tSNR (bottom row) in a whole brain volume between EPI with noDC, SDC and DDC, where there was intentional motion (rotations up to 6.7°, 7.1° and 8.1° for V1, V2 and V3 respectively). Insets in the upper right corner of each graph show the same results on a logarithmic scale.

strong signal decay and in slices with disconnected tissue. At 3 T and below phase unwrapping can be avoided by calculating only relative phase changes in the EPI time series (Hahn et al., 2009; Ooi et al., 2012). In our experiments at 7 T, head rotations of about 0.6° induced phase differences larger than 2π in brain regions with strong field inhomogeneities, creating phase wraps and eliminating this alternative solution. We have proposed a multi-step approach consisting of triplanar unwrapping using 2D PRELUDE, smoothing with extrapolation and a congruence operation. This led to correct unwrapping in all images except in a region of a few voxels at the brain boundary in subject V1 (see Fig. S1, arrow nr 1). This corresponded to rotation of 7.9°, however, which is above the motion typical in fMRI studies. We have tested several most commonly used unwrapping methods, including 2D and 3D PRELUDE, Cusack's method (Cusack and Papadakis, 2002), PHUN (Witoszynskyj et al., 2009), branch cut approach (Goldstein et al., 1988) and weighted Laplacian unwrapping with a congruence operation (Ghiglia and Pritt, 1998). All these methods led to substantially larger unwrapping errors than the approach proposed here. In addition to robustness, the outcome from this multi-step procedure is characterized by a smooth background which is well-suited for distortion correction as it reduces the problem of shifting noise values to the inside of the brain, which occurs in unwarping if voxels with a high noise level are present close to brain boundaries. In practice it means that the masking of field maps is not necessary.

We present the first investigation, to our knowledge, of the temporal stability of phase offsets at 7 T. Experiment 1 showed that $\varphi_{0,ch}$ were not changed by the intensive switching of the gradients during 40 min of EPI acquisition at 7 T and Experiment 2 that $\varphi_{0,ch}$ were stable in the presence of large motion. These conclusions are based on the errors in DDC which would arise from changes in $\varphi_{0,ch}$, which were estimated to reach the maximum of -0.2 voxels for the head rotations up to 12°. A SDC would lead to errors of up to 11.4 voxels for the same motion. The errors in static unwarping were generally 1–2 orders of magnitude larger than in our dynamic unwrapping method for the same head motion.

The DDC approach proposed accurately corrected geometric distortions even in the presence of large head rotation. The SDC, on the other hand, led to substantial errors (e.g. up to 11.2 mm for 6.7° rotation), even exacerbating distortion for head rotations of a few degrees and blurring gray/white matter boundaries (see Fig. S2 in circle). Modest head rotation of 0.8° led to errors of 6.4 mm in SDC (see Fig. 3, arrow 1). Original EPI and SDC EPI showed a gradual stretching of the image in the phase encoding direction with head rotation which was effectively corrected with the dynamic method (see movie in Supplementary material), leading to increased tSNR and, consequently, BOLD sensitivity (Parrish et al., 2000; Triantafyllou et al., 2005).

The DDC approach proposed accurately corrected geometric distortions even in the presence of large head rotation. The SDC, on the other hand, led to substantial errors (e.g. up to 11.2 mm for 6.7° rotation), even exacerbating distortion for head rotations of a few degrees and blurring gray/white matter boundaries (see Fig. S2 in circle). Modest head rotation of 0.8° led to errors of 6.4 mm in SDC (see Fig. 3, arrow 1). Original EPI and SDC EPI showed a gradual stretching of the image in the phase encoding direction with head rotation which was effectively corrected with the dynamic method (see movie in Supplementary material), leading to increased tSNR and, consequently, BOLD sensitivity (Parrish et al., 2000; Triantafyllou et al., 2005).

Motion correction is generally improved if DDC is performed as a prior step (Hahn et al., 2009). This was also observed here; motion correction failed completely at rotations above 8° for original and SDC data, but not for dynamically corrected images. Our analysis extends to motion which is larger than that which would typically be deemed acceptable in basic neuroscience studies (Gracco et al., 2005). Such motion may occur in presurgical planning (Krings et al., 2001; Sunaert, 2006), causing dynamic distortions potentially affecting surgical decisions (Dymerska et al., 2014), or in studies of patients with Parkinson's, Alzheimer's, epilepsy, hyperkinesia or post stroke (Lemieux et al., 2007; Seto et al., 2001).

The analysis of the quality of the dynamic distortion correction (Exp. 3) was performed on small number of healthy volunteers (3),

for which results for the DDC method were consistent, showing high geometric accuracy of the correction and increased temporal stability in the case of motion. Anatomical differences in other volunteers or patients could create new challenges, especially in the phase unwrapping process. This work represents a proof of principle; a thorough testing on a larger group of subjects is necessary to confirm the robustness of the proposed method, especially in pathological brains.

The data presented here were acquired using GRAPPA reconstruction (Griswold et al., 2002). In a SENSE reconstruction (Pruessmann et al., 1999), separate channel phase matching is performed with respect to a reference coil such as a body coil. Phase images reconstructed with SENSE comprise both the desired ΔB_0 contribution and a second contribution arising from the transmit and receive B_1 of the reference coil. This reference coil phase offset contribution can be determined from dual-echo GE data acquired with the reference coil (using Eqs. (6) and (7), for a single channel), and subtracted.

Our DDC approach can be used with parallel imaging (Griswold et al., 2002; Pruessmann et al., 1999), as in accelerated 2D EPI, 3D EPI (Poser et al., 2010) and simultaneous multi-slice acquisitions (Larkman et al., 2001; Setsompop et al., 2012). These techniques are being used at UHF to measure human brain activity at the level of cortical layers and columnar clusters, i.e. to examine mesoscopic functional brain organization with sub-millimeter spatial resolution (Heidemann et al., 2012; Koopmans et al., 2011; Nasr et al., 2016; Sánchez-Panchuelo et al., 2012; Yacoub et al., 2008; Zimmermann et al., 2011). Our DDC method can aid accurate coregistration of function and structure in such high resolution studies, which tend to suffer from increased geometric distortions due to increased echo spacing.

Functional MRI is predominantly based on analysis of the magnitude signal. New insights into micro- and macrovascular BOLD signal contributions can be won from the complex signal (Calhoun et al., 2002; Menon, 2002; Rowe, 2005) or the phase in isolation, however, as in functional Quantitative Susceptibility Mapping (fQSM) (Balla et al., 2014; Bilgic et al., 2014). The field maps described in this study are scaled, combined phase images which can be used for fQSM or complex signal functional analysis. As such, our approach to single-echo DDC also represents a solution to the problem of combining multi-channel phase information (Robinson et al., 2015) for EPI time series. Phase images generated with this method can also be used for physiological monitoring, since temperature changes, respiration and cardiac fluctuations cause dynamic changes in phase (Ishihara et al., 1995; Zahneisen et al., 2014). It may be possible to distinguish between different contributions to the phase signal (of BOLD origin or motion, temperature or respiration-related) using, Independent Component Analysis (Calhoun et al., 2002; Robinson et al., 2013), for instance.

Conclusion

We have proposed a method for correcting B_0-related distortions in single-echo EPI which is applicable in fMRI with multi-channel coils at ultra-high fields (7 T). Phase offsets estimated from a short dual-echo GE acquisition are used to obtain maps of field inhomogeneities at each time point in an EPI time series. EPI which were distortion-corrected using this dynamic approach were geometrically true to distortion-free reference scans and had increased temporal SNR, especially in the presence of large motion. This method can be applied to all fMRI studies that use single-echo EPI, but is of particularly high interest in presurgical planning, high resolution studies, functional Quantitative Susceptibility Mapping and the monitoring of physiological effects related to temperature, respiration and cardiac fluctuations.

Supplementary data to this article can be found online at http://dx.doi.org/10.1016/j.neuroimage.2016.07.009.

Acknowledgements

This study was funded by a DOC fellowship of the Austrian Academy of Science. Additional support was provided by the Austrian Science Fund (FWF KLI 264).

References

Andersson, J.L.R., Hutton, C., Ashburner, J., Turner, R., Friston, K., 2001. Modeling geometric deformations in EPI time series. NeuroImage 13, 903–919. http://dx.doi.org/10.1006/nimg.2001.0746.

Balla, D.Z., Sanchez-Panchuelo, R.M., Wharton, S.J., Hagberg, G.E., Scheffler, K., Francis, S.T., Bowtell, R., 2014. Functional quantitative susceptibility mapping (fQSM). NeuroImage 100, 112–124. http://dx.doi.org/10.1016/j.neuroimage.2014.06.011.

Beisteiner, R., Robinson, S., Wurnig, M., Hilbert, M., Merksa, K., Rath, J., Höllinger, I., Klinger, N., Marosi, C., Trattnig, S., Geißler, A., 2011. Clinical fMRI: evidence for a 7 T benefit over 3 T. NeuroImage 57, 1015–1021. http://dx.doi.org/10.1016/j.neuroimage.2011.05.010.

Bernstein, M.A., Grgic, M., Brosnan, T.J., Pelc, N.J., 1994. Reconstructions of phase contrast, phased array multicoil data. Magn. Reson. Med. 32, 330–334. http://dx.doi.org/10.1002/mrm.1910320308.

Bilgic, B., Fan, A.P., Polimeni, J.R., Cauley, S.F., Bianciardi, M., Adalsteinsson, E., Wald, L.L., Setsompop, K., 2014. Fast quantitative susceptibility mapping with L1-regularization and automatic parameter selection. Magn. Reson. Med. 72, 1444–1459. http://dx.doi.org/10.1002/mrm.25029.

Calhoun, V.D., Adalı, T., Pearlson, G.D., van Zijl, P.C.M., Pekar, J.J., 2002. Independent component analysis of fMRI data in the complex domain. Magn. Reson. Med. 48, 180–192. http://dx.doi.org/10.1002/mrm.10202.

Collins, C.M., 2006. Radiofrequency field calculations for high field MRI, Ultra High Field Magnetic Resonance Imaging, Biological Magnetic Resonance. Springer US, pp. 209–248.

Cusack, R., Papadakis, N., 2002. New robust 3-D phase unwrapping algorithms: application to magnetic field mapping and undistorting echoplanar images. NeuroImage 16, 754–764.

Cusack, R., Brett, M., Osswald, K., 2003. An evaluation of the use of magnetic field maps to undistort echo-planar images. NeuroImage 18, 127–142.

De Panfilis, C., Schwarzbauer, C., 2005. Positive or negative blips? The effect of phase encoding scheme on susceptibility-induced signal losses in EPI. NeuroImage 25, 112–121. http://dx.doi.org/10.1016/j.neuroimage.2004.11.014.

Dymerska, B., Fischmeister, F.P.S., Geissler, A., Matt, E., Trattnig, S., Beisteiner, R., Robinson, S.D., 2014. Clinical relevance of EPI distortion correction in presurgical fMRI at 7 Tesla, Proc. Twenty-Third Annu. Meet. ISMRM 2014 Milan #1416.

Dymerska, B., Poser, B.A., Bogner, W., Visser, E., Eckstein, K., Cardoso, P., Barth, M., Trattnig, S., Robinson, S.D., 2015. Correcting dynamic distortions in 7 T echo planar imaging using a jittered echo time sequence. Magn. Reson. Med. . http://dx.doi.org/10.1002/mrm.26018

Foerster, B.U., Tomasi, D., Caparelli, E.C., 2005. Magnetic field shift due to mechanical vibration in functional magnetic resonance imaging. Magn. Reson. Med. 54, 1261–1267. http://dx.doi.org/10.1002/mrm.20695.

Garcia, D., 2010. Robust smoothing of gridded data in one and higher dimensions with missing values. Comput. Stat. Data Anal. 54, 1167–1178. http://dx.doi.org/10.1016/j.csda.2009.09.020.

Gartus, A., Geissler, A., Foki, T., Tahamtan, A.R., Pahs, G., Barth, M., Pinker, K., Trattnig, S., Beisteiner, R., 2006. Comparison of fMRI coregistration results between human experts and software solutions in patients and healthy subjects. Eur. Radiol. 17, 1634–1643. http://dx.doi.org/10.1007/s00330-006-0459-z.

Ghiglia, D.C., Pritt, M.D., 1998. Two-Dimensional Phase Unwrapping: Theory, Algorithms, and Software. Wiley.

Goldstein, R.M., Zebker, H.A., Werner, C.L., 1988. Satellite radar interferometry: two-dimensional phase unwrapping. Radio Sci. 23, 713–720. http://dx.doi.org/10.1029/RS023i004p00713.

Gracco, V.L., Tremblay, P., Pike, B., 2005. Imaging speech production using fMRI. NeuroImage 26, 294–301. http://dx.doi.org/10.1016/j.neuroimage.2005.01.033.

Griswold, M.A., Jakob, P.M., Heidemann, R.M., Nittka, M., Jellus, V., Wang, J., Kiefer, B., Haase, A., 2002. Generalized autocalibrating partially parallel acquisitions (GRAPPA). Magn. Reson. Med. 47, 1202–1210. http://dx.doi.org/10.1002/mrm.10171.

Hahn, A.D., Nencka, A.S., Rowe, D.B., 2009. Improving robustness and reliability of phase-sensitive fMRI analysis using temporal off-resonance alignment of single-echo timeseries (TOAST). NeuroImage 44, 742–752. http://dx.doi.org/10.1016/j.neuroimage.2008.10.001.

Heidemann, R.M., Ivanov, D., Trampel, R., Fasano, F., Meyer, H., Pfeuffer, J., Turner, R., 2012. Isotropic submillimeter fMRI in the human brain at 7 T: combining

reduced field-of-view imaging and partially parallel acquisitions. Magn. Reson. Med. 68, 1506–1516. http://dx.doi.org/10.1002/mrm.24156.
Hutton, C., Bork, A., Josephs, O., Deichmann, R., Ashburner, J., Turner, R., 2002. Image distortion correction in fMRI: a quantitative evaluation. NeuroImage 16, 217–240.
Hutton, C., Andersson, J., Deichmann, R., Weiskopf, N., 2013. Phase informed model for motion and susceptibility. Hum. Brain Mapp. 34, 3086–3100. http://dx.doi.org/10.1002/hbm.22126.
Ishihara, Y., Calderon, A., Watanabe, H., Okamoto, K., Suzuki, Y., Kuroda, K., Suzuki, Y., 1995. A precise and fast temperature mapping using water proton chemical shift. Magn. Reson. Med. 34, 814–823. http://dx.doi.org/10.1002/mrm.1910340606.
Jenkinson, M., 2003. Fast, automated, N-dimensional phase-unwrapping algorithm. Magn. Reson. Med. 49, 193–197. http://dx.doi.org/10.1002/mrm.10354.
Jezzard, P., Balaban, R.S., 1995. Correction for geometric distortion in echo planar images from B0 field variations. Magn. Reson. Med. 34, 65–73. http://dx.doi.org/10.1002/mrm.1910340111.
Jezzard, P., Clare, S., 1999. Sources of distortion in functional MRI data. Hum. Brain Mapp. 8, 80–85.
Koopmans, P.J., Barth, M., Orzada, S., Norris, D.G., 2011. Multi-echo fMRI of the cortical laminae in humans at 7 T. NeuroImage 56, 1276–1285. http://dx.doi.org/10.1016/j.neuroimage.2011.02.042.
Krings, T., Reinges, M.H.T., Erberich, S., Kemeny, S., Rohde, V., Spetzger, U., Korinth, M., Willmes, K., Gilsbach, J.M., Thron, A., 2001. Functional MRI for presurgical planning: problems, artefacts, and solution strategies. J. Neurol. Neurosurg. Psychiatry 70, 749–760. http://dx.doi.org/10.1136/jnnp.70.6.749.
Lamberton, F., Delcroix, N., Grenier, D., Mazoyer, B., Joliot, M., 2007. A new EPI-based dynamic field mapping method: application to retrospective geometrical distortion corrections. J. Magn. Reson. Imaging 26, 747–755. http://dx.doi.org/10.1002/jmri.21039.
Larkman, D.J., Hajnal, J.V., Herlihy, A.H., Coutts, G.A., Young, I.R., Ehnholm, G., 2001. Use of multicoil arrays for separation of signal from multiple slices simultaneously excited. J. Magn. Reson. Imaging 13, 313–317. http://dx.doi.org/10.1002/1522-2586(200102)13:2<313::AID-JMRI1045>3.0.CO;2-W.
Lemieux, L., Salek-Haddadi, A., Lund, T.E., Laufs, H., Carmichael, D., 2007. Modelling large motion events in fMRI studies of patients with epilepsy. Magn. Reson. Imaging 25, 894–901. http://dx.doi.org/10.1016/j.mri.2007.03.009.
Marques, J.P., Bowtell, R., 2005. Evaluation of a new method to correct the effects of motion-induced B0-field variation during fMRI, Proc. 13th Annu. Meet. ISMRM 510.
Menon, R.S., 2002. Postacquisition suppression of large-vessel BOLD signals in high-resolution fMRI. Magn. Reson. Med. 47, 1–9. http://dx.doi.org/10.1002/mrm.10041.
MRIcro [WWW Document], . (n.d. URL) http://people.cas.sc.edu/rorden/mricro/index.html (accessed 4.26.16).
Nasr, S., Polimeni, J.R., Tootell, R.B.H., 2016. Interdigitated color- and disparity-selective columns within human visual cortical areas V2 and V3. J. Neurosci. 36, 1841–1857. http://dx.doi.org/10.1523/JNEUROSCI.3518-15.2016.
Ooi, M.B., Muraskin, J., Zou, X., Thomas, W.J., Krueger, S., Aksoy, M., Bammer, R., Brown, T.R., 2012. Combined prospective and retrospective correction to reduce motion-induced image misalignment and geometric distortions in EPI. Magn. Reson. Med. 69 (3), 803–811. http://dx.doi.org/10.1002/mrm.24285.
Parrish, T.B., Gitelman, D.R., LaBar, K.S., Mesulam, M.-M., 2000. Impact of signal-to-noise on functional MRI. Magn. Reson. Med. 44, 925–932. http://dx.doi.org/10.1002/1522-2594(200012)44:6<925::AID-MRM14>3.0.CO;2-M.
Poser, B.A., Norris, D.G., 2009. Investigating the benefits of multi-echo EPI for fMRI at 7 T. NeuroImage 45, 1162–1172. http://dx.doi.org/10.1016/j.neuroimage.2009.01.007.
Poser, B.A., Koopmans, P.J., Witzel, T., Wald, L.L., Barth, M., 2010. Three dimensional echo-planar imaging at 7 Tesla. NeuroImage 51, 261–266. http://dx.doi.org/10.1016/j.neuroimage.2010.01.108.
Pruessmann, K.P., Weiger, M., Scheidegger, M.B., Boesiger, P., 1999. SENSE: sensitivity encoding for fast MRI. Magn. Reson. Med. 42, 952–962.
Reeder, S.B., Atalar, E., Faranesh, A.Z., McVeigh, E.R., 1999. Referenceless interleaved echo-planar imaging. Magn. Reson. Med. 41, 87–94. http://dx.doi.org/10.1002/(SICI)1522-2594(199901)41:1<87::AID-MRM13>3.0.CO;2-X.
Robinson, S., Jovicich, J., 2011. B0 mapping with multi-channel RF coils at high field. Magn. Reson. Med. 66, 976–988. http://dx.doi.org/10.1002/mrm.22879.
Robinson, S., Grabner, G., Witoszynskyj, S., Trattnig, S., 2011. Combining phase images from multi-channel RF coils using 3D phase offset maps derived from a dual-echo scan. Magn. Reson. Med. 65, 1638–1648. http://dx.doi.org/10.1002/mrm.22753.
Robinson, S.D., Schöpf, V., Cardoso, P., Geissler, A., Fischmeister, F.P.S., Wurnig, M., Trattnig, S., Beisteiner, R., 2013. Applying independent component analysis to clinical fMRI at 7 T. Front. Hum. Neurosci. 7, 496. http://dx.doi.org/10.3389/fnhum.2013.00496.
Robinson, S., Dymerska, B., Trattnig, S., 2014. Improving the accuracy of 2D phase unwrapping using a triplanar approach, Proc. 22nd Annu. Meet. ISMRM Milan #3262.
Robinson, S.D., Dymerska, B., Bogner, W., Barth, M., Zaric, O., Goluch, S., Grabner, G., Deligianni, X., Bieri, O., Trattnig, S., 2015. Combining phase images from array coils using a short echo time reference scan (COMPOSER). Magn. Reson. Med. . http://dx.doi.org/10.1002/mrm.26093 (n/a-n/a)
Rowe, D.B., 2005. Modeling both the magnitude and phase of complex-valued fMRI data. NeuroImage 25, 1310–1324.
Sánchez-Panchuelo, R.M., Francis, S.T., Schluppeck, D., Bowtell, R.W., 2012. Correspondence of human visual areas identified using functional and anatomical MRI in vivo at 7 T. J. Magn. Reson. Imaging 35, 287–299. http://dx.doi.org/10.1002/jmri.22822.
Seto, E., Sela, G., McIlroy, W.E., Black, S.E., Staines, W.R., Bronskill, M.J., McIntosh, A. R., Graham, S.J., 2001. Quantifying head motion associated with motor tasks used in fMRI. NeuroImage 14, 284–297. http://dx.doi.org/10.1006/nimg.2001.0829.
Setsompop, K., Gagoski, B.A., Polimeni, J.R., Witzel, T., Wedeen, V.J., Wald, L.L., 2012. Blipped-controlled aliasing in parallel imaging for simultaneous multislice echo planar imaging with reduced g-factor penalty. Magn. Reson. Med. 67, 1210–1224. http://dx.doi.org/10.1002/mrm.23097.
Smith, S.M., 2002. Fast robust automated brain extraction. Hum. Brain Mapp. 17, 143–155. http://dx.doi.org/10.1002/hbm.10062.
Sunaert, S., 2006. Presurgical planning for tumor resectioning. J. Magn. Reson. Imaging 23, 887–905. http://dx.doi.org/10.1002/jmri.20582.
Triantafyllou, C., Hoge, R.D., Krueger, G., Wiggins, C.J., Potthast, A., Wiggins, G.C., Wald, L.L., 2005. Comparison of physiological noise at 1.5 T, 3 T and 7 T and optimization of fMRI acquisition parameters. NeuroImage 26, 243–250. http://dx.doi.org/10.1016/j.neuroimage.2005.01.007.
van der Zwaag, W., Francis, S., Head, K., Peters, A., Gowland, P., Morris, P., Bowtell, R., 2009. fMRI at 1.5, 3 and 7 T: characterising BOLD signal changes. NeuroImage 47, 1425–1434. http://dx.doi.org/10.1016/j.neuroimage.2009.05.015.
Vegh, V., O'Brien, K., Barth, M., Reutens, D.C., 2015. Selective channel combination of MRI signal phase. Magn. Reson. Med. . http://dx.doi.org/10.1002/mrm.26057
Visser, E., Poser, B.A., Barth, M., Zwiers, M.P., 2012. Reference-free unwarping of EPI data using dynamic off-resonance correction with multiecho acquisition (DOCMA). Magn. Reson. Med. 68, 1247–1254. http://dx.doi.org/10.1002/mrm.24119.
Weiskopf, N., Klose, U., Birbaumer, N., Mathiak, K., 2005. Single-shot compensation of image distortions and BOLD contrast optimization using multi-echo EPI for real-time fMRI. NeuroImage 24, 1068–1079. http://dx.doi.org/10.1016/j.neuroimage.2004.10.012.
Wharton, S., Bowtell, R., 2012. Fiber orientation-dependent white matter contrast in gradient echo MRI. Proc. Natl. Acad. Sci. U. S. A. 109, 18559–18564. http://dx.doi.org/10.1073/pnas.1211075109.
Witoszynskyj, S., Rauscher, A., Reichenbach, J.R., Barth, M., 2009. Phase unwrapping of MR images using Phi UN–a fast and robust region growing algorithm. Med. Image Anal. 13, 257–268. http://dx.doi.org/10.1016/j.media.2008.10.004.
Yacoub, E., Harel, N., Uğurbil, K., 2008. High-field fMRI unveils orientation columns in humans. Proc. Natl. Acad. Sci. 105, 10607–10612. http://dx.doi.org/10.1073/pnas.0804110105.
Zahneisen, B., Assländer, J., LeVan, P., Hugger, T., Reisert, M., Ernst, T., Hennig, J., 2014. Quantification and correction of respiration induced dynamic field map changes in fMRI using 3D single shot techniques. Magn. Reson. Med. 71, 1093–1102. http://dx.doi.org/10.1002/mrm.24771.
Zeller, M., Kraus, P., Müller, A., Bley, T.A., Köstler, H., 2013. Respiration impacts phase difference-based field maps in echo planar imaging. Magn. Reson. Med. 72, 446–451. http://dx.doi.org/10.1002/mrm.24938.
Zimmermann, J., Goebel, R., Martino, F.D., van de Moortele, P.F., Feinberg, D., Adriany, G., Chaimow, D., Shmuel, A., Uğurbil, K., Yacoub, E., 2011. Mapping the organization of axis of motion selective features in human area MT using high-field fMRI. PLoS One 6, e28716. http://dx.doi.org/10.1371/journal.pone.0028716.